Cathode and Anode Materials for Na-Ion Battery

Lifen Xao, Yuliang Cao and Jun Liu

Abstract Energy storage is more important today than at any time in the human history. The battery systems that are pursued for clean renewable energy-based grid or the electrification of transportation need to meet the requirements of low cost and high efficiency. Li-ion battery is the most advanced battery system, but it is expensive and insufficient as a resource for widespread application. Na-ion battery is seen as a promising alternative due to the abundance of Na resource. However, the realization of the Na-ion intercalation/deintercalation mechanism is also challenging because Na ions are 40 % larger in radius than Li ions. This makes the finding of suitable host materials with high storage capacity, rapid ion uptaking rate, and long cycling life not easy. In the recent 3 years, several electrode materials were found to have energy density close to those used in Li-ion batteries. These scientific advances have greatly rekindled worldwide passion for Na-ion battery system. In this chapter, the development of the electrode materials for Na-ion batteries is briefly reviewed, with the aim of providing a wide view of the problems and future research orientations of this system.

L. Xao
College of Chemistry, Central China Normal University, Wuhan 430079, People's Republic of China

Y. Cao
College of Chemistry and Molecular Science, Wuhan University, Wuhan 430072, People's Republic of China

J. Liu (✉)
Pacific Northwest National Laboratory, Richland, WA 99352, USA
e-mail: Jun.Liu@pnnl.gov

Z. Lin and J. Wang (eds.), *Low-cost Nanomaterials*, Green Energy and Technology,
DOI: 10.1007/978-1-4471-6473-9_14,

1 Introduction

Energy is not only the material foundation that sustains the advance of human civilization, but also the indispensable requirement for the development of modern society. With the rapid growth of the global economy, our society has become increasingly interdependent on energy. As data show 70 % of the world's annual energy consumption comes from fossil fuels, there can be no doubt that our reserves of fossil fuels are finite, and the resulting environmental pollution is worsening. Thus, we need to promote the harnessing of clean, renewable energy sources such as solar, wind, geothermal, and tidal energy. However, these renewable resources are commonly intermittent in time and diffusive in space; the electricity produced must be stored and made available on demand. So large-scale electric energy storage (EES) systems will be an essential part of the future renewable energy-based grid. Meanwhile, another pressing demand is to find appropriate EES for the electrification of transportation that does not emit greenhouse gases.

Electrochemistry can contribute to EES in several diverse ways. Electrochemical energy storage technologies include flow redox batteries, super capacitors, and rechargeable batteries (Pb–acid, Ni–Cd, Na–S, and Li-ion batteries, etc.), showing great advantages of high efficiency, low cost, and flexibility. Hereinto, Li-ion batteries have currently been considered as one of the most promising technologies due to their long lifetime and high energy density. However, for widespread EES applications, there is increasing concern about the cost and limitation of lithium terrestrial reserves. As a result, great efforts have been made to explore new low-cost and reliable electrochemical energy storage technologies.

Due to the global lithium resource constraint, scientists have turned their attention to rechargeable Na-based batteries. As Na is positioned in the same period with Li, its electrochemical properties are similar to Li. Na has very negative redox potential (–2.71 V, vs. SHE) and a small electrochemical equivalent (0.86 gAh^{-1}), which makes it the most advantageous element for battery applications after lithium. Na element instead has very abundant and widespread supply as the crustal abundance of Na is 2.64 %, compared to 0.006 % of Li. Moreover, there is 3.5 % of NaCl in the ocean, showing inexhaustible Na resource, thus Na is an ideal energy storage material.

In the past decades, high-temperature Na battery system such as Na/S and Na/$NiCl_2$ (ZEBRA battery) systems have been commercially developed for electric vehicles and MWh scale electric storage due to their high energy density and low cost. Na/S batteries produced by NGK Ltd. in Japan have entered in the market since 2000. The biggest units with a power output of 8 MW have been built and more than a hundred Na/S energy storage stations are operating over the globe. The biggest market of ZEBRA batteries is thought to be transportation. Benz Corp in German has carried out longtime tests since the 1990s, where the index of the ZEBRA batteries can fulfill the medium-term target of USABC. The ZEBRA battery powered vehicles have passed over 3,200 thousand miles' test.

A major obstacle hindering the broad market penetration of these two types of Na batteries is the long-term stability and endurance of the battery components at high temperatures of ≥300°C.

2 Na-Ion Batteries and Problems

If a room temperature Na-ion rocking chair battery (Na-ion battery) (Fig. 1) can be achieved, it would bring about great improvement in safety and operational simplicity with respect to the conventional high-temperature Na batteries and also a remarkable decrease in cost with regard to Li-ion batteries, thus ensuring sustainable applications for large-scale electric energy storage. Since Na-ion batteries have the similar working principle as Li-ion batteries, the development of this system would benefit greatly from the knowledge as well as configurations gained within Li-ion batteries. However, it should be noted that: 1. the gravimetric capacity of Na is lower (1,165 mAh g^{-1}) than lithium (3,829 mAh g^{-1}) due to its larger molecular mass [1]. Thus, the Na-ion battery system will achieve lower energy density than Li-ion batteries. 2. Na ions are about 40 % larger than Li ions in radius, which make them more stable in rigid lattices [1]. Thus, it will be harder to find proper materials that are able to realize reversible Na storage and release. Due to its large dimensions, the insertion and extraction of Na ions can arouse more serious stress changes of the host materials, causing rapid collapse of lattice structure and therefore poor cycling stability. The diffusion of Na-ions in lattice is also slow, resulting in poor electrochemical utilization and rate capability. 3. Na metal is more chemically active than Li, which needs very strict restriction of the moisture and oxygen content on the experimental environment. In this chapter, recent research progress in electrode materials is reviewed for Na-ion batteries. The practical specific capacity and operating voltage of some of the electrode materials for Na-ion battery are summarized in Fig. 2.

3 Cathode Materials for Na-Ion Batteries

The electrochemical performance of Na-ion batteries mainly depends on the structures and properties of electrode materials and electrolytes. As one of the key components of Na-ion batteries, suitable cathode materials should meet the following requirements:

1. High redox potential, which is less influenced by the concentration of Na ions in the lattices, to maintain high and even charge/discharge voltage.
2. Small electrochemical equivalent, i.e., light molecular weight and more electrons transferred per unit of the active material, to provide high specific capacity.

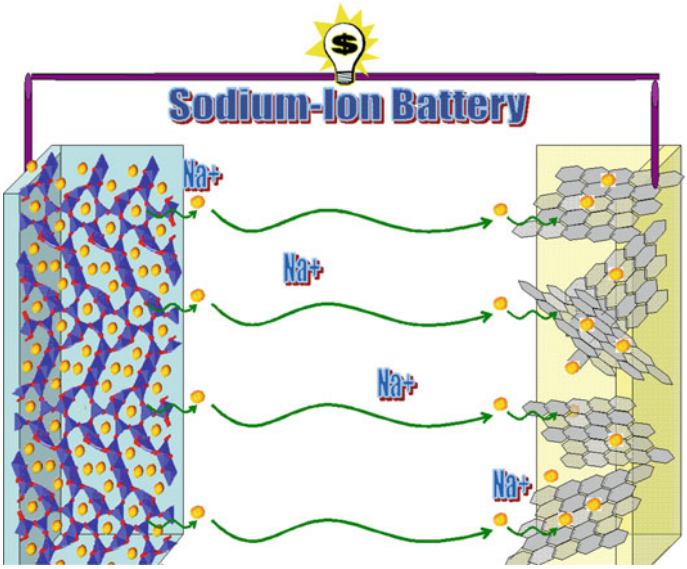

Fig. 1 Schematic diagram of Na-ion battery

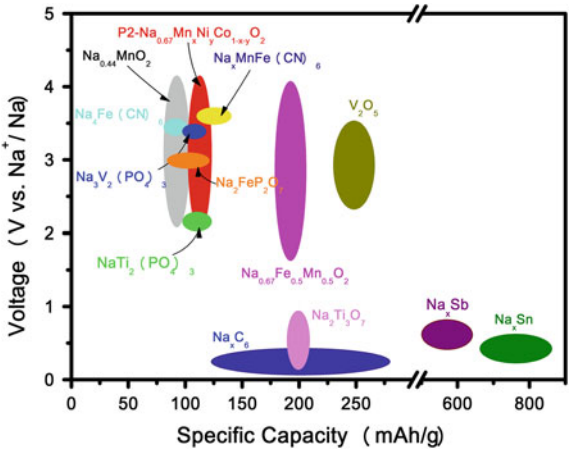

Fig. 2 Pratical specific capacity and operating voltage in current Na-ion battery technologies

3. High structural and chemical stability to ensure good cyclability.
4. High electronic and Na-ion conductivity to realize rapid charge/discharge.
5. Mass production convenient, resource abundant, and environment benign.

A wide variety of compounds have been investigated for cathodes used in Na-ion batteries. In this section, we mainly focus on metal oxides, polyanion compounds, and metal hexacyanides.

3.1 Metal Oxides

Li metal oxide materials ($LiCoO_2$, $LiNi_xCo_yMn_{1-x-y}O_2$, $LiMn_2O_4$, etc.) have been widely investigated as Li-ion intercalation hosts. These materials exhibit good capacity and structural stability during repeated Li-ion insertion/extraction cycles. Analogously, Na-based metal oxides also have similar formula and crystal structure with Li-based oxides. Indeed, these metal oxides have been first considered as Na-ion hosts. Some typical crystal structures of Na-based metal oxides are illustrated in Fig. 3. Three types of layered structures (Fig. 3a–c) can be denoted as On or Pn (n = 1, 2, 3,…), depending on the insertion environment of alkali atoms and the repeat period (n) of the transition metal oxide (MO) sheets forming MO_6 edge-sharing octahedra [3]. Na atoms lie in the octahedral sites in O3 structure (Fig. 3a) while occupy the trigonal prismatic sites in P2 and P3 structures (Fig. 3b, c). Therefore, phase transitions between O3 and P3 will occur due to the movement of Na atoms from the octahedral sites to the trigonal prismatic sites along with the gliding of MO sheets. The phase transitions cause the multi-voltage plateaus of the layered Na_xMO_2 material during charge/discharge. However, the phase transitions between O3 and P2 cannot occur at room temperature because of the high cleavage energy of the M–O bonds [2]. In general, O3-type metal oxides can extract more Na atoms (hence discharge capacity) from the crystal structure; P2-type metal oxides have higher structural stability during repeated charge/discharge. Some other metal oxides have a three-dimensional tunnel structure such as orthorhombic $Na_{0.44}MnO_2$ shown in Fig. 3d. $Na_{0.44}MnO_2$ is made of MnO_5 square pyramids and MnO_6 octahedra, which are arranged to form two types of tunnels: large S-shaped tunnels and smaller pentagon tunnels (Fig. 3d). Na atoms can intercalate into these tunnels. 3D tunnels usually can not only offer stable structure to allow free movement of Na ions inside the crystal structure, but also provide fast channels for Na ion moving in/out of the crystal structure [4–7].

3.1.1 Na_xCoO_2

In the early 1980s, Na_xCoO_2 has been studied as cathode materials for Na batteries [8]. Braconnier et al. reported that Na_xCoO_2 has four different phases, O3 ($0.9 < x < 1$), O′3 ($x = 0.75$), P3 ($0.55 < x < 0.6$), and P2 ($0.64 < x < 0.74$) depending on the concentration of Na ions. Among them, P2–$Na_{0.7}CoO_2$ (Fig. 1b) shows the largest energy density (260 Wh kg^{-1}). Recently, Delmas et al. used Na batteries to convey a thorough investigation of the P2–Na_xCoO_2 phase diagram for $x \geq 0.50$ (Fig. 4). It showed a succession of single phases or two-phase domains on Na ion intercalation [9]. Harharan et al. investigated the effect of synthesis methods on the electrochemical performance of P2–$Na_{0.7}CoO_2$ [10]. They found the sample prepared by sol–gel method has the highest discharge capacity (10 and 50 % higher than those prepared by solid state reaction and high-energy ball milling methods), due to the smaller particular size and larger surface area.

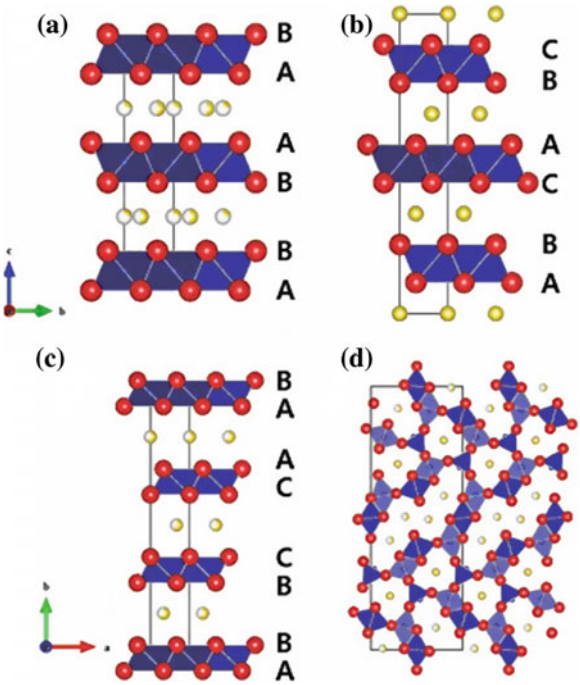

Fig. 3 Crystal structures of various Na_xMO_y: **a** P2–Na_xCoO_2 **b** O3–Na_xCoO_2**c** P3–Na_xCoO_2, and **d** $Na_{0.44}MnO_2$ (Na: *yellow*, Co/Mn/V: *blue*, O: *red*) [2]

Though $LiCoO_2$ is the hottest commercial cathode material for Li-ion battery, Na_xCoO_2 unfortunately cannot match a good cathode either in energy density or in cyclability for Na ion batteries. Besides, Co as a precious metal does not meet the low-cost demand of Na-ion battery.

3.1.2 Na_xMnO_2

In the early 1970s, Mn–O–Na ternary system has been widely investigated and a wide structural Na_xMnO_2 (depending strongly on the concentration of Na and the preparation condition) has been reported [11]. The most typical structures are α–$NaMnO_2$ with lamellar structure of O′3 type (Fig. 3a), $Na_{0.7}MnO_2$ with lamellar structure of P2 type (Fig. 3b), and $Na_{0.44}MnO_2$ with three-dimensional channel structure (Fig. 3d). Delmas et al. studied the Na intercalation behavior in the above three types of Na_xMnO_2. They found that within a certain range of x ($0.45 \leq x \leq 0.85$ for α–$NaMnO_2$ and $Na_{0.70}MnO_2$, $0.30 \leq x \leq 0.58$ for $Na_{0.44}MnO_2$), these materials can maintain very well their pristine structures, showing potential to be used as cathode materials for Na-ion batteries. Caballero et al. [12] prepared P2–$Na_{0.6}MnO_2$ by using sol–gel method, which showed high purity and a well-defined layered structure (Fig. 3b). The material delivered a high specific capacity of *ca.* 140 mAh g^{-1} (corresponding to an intercalation amount of ~0.52) during the initial several cycles, and then the capacity declined on

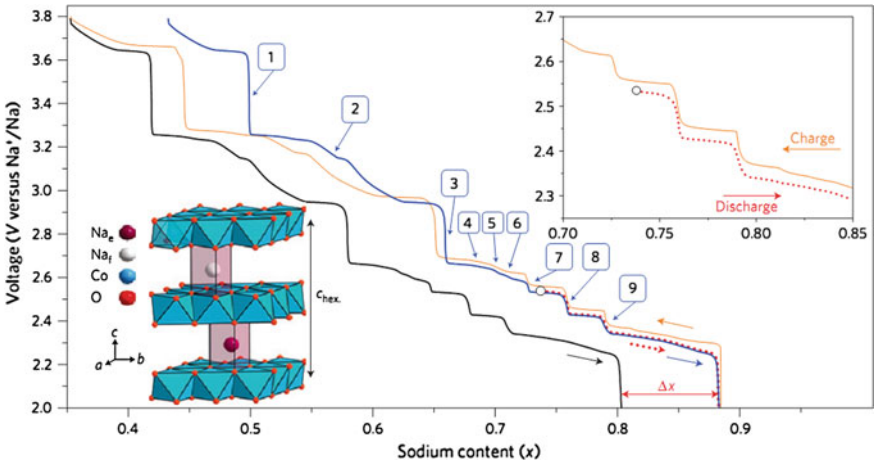

Fig. 4 Galvanostatic cycling curve of an Na/P2–Na_xCoO_2 battery giving an overview of the phase diagram [9]

successive cycles. It was considered that the intercalation/deintercalation of Na ions can cause repeated gliding of the MO sheets, leading to collapse of the layered structure into amorphous after the first eight cycles [12]. So, the structural stability is still an issue on the layered Na_xMnO_2 material.

Compared to layered Na_xMnO_2, orthorhombic $Na_{0.44}MnO_2$ shows higher stability in structure, the MnO_6 octahedra, and MnO_5 square pyramids form a framework possessing two types of Na-ion diffusion channels (Fig. 3d): large S-shaped tunnels and smaller pentagon tunnels. Na ions occupy three sites in this structure: the Na(1) site in the small tunnels is fully occupied while the Na(2) and Na(3) sites in the large S-shaped tunnels are half occupied. Na ions in the large S-shaped tunnels can be extracted, while Na ions in the small tunnels are immovable due to the small tunnel size and strong interaction with the surrounding oxygen atoms. Sauvage et al. synthesized well-crystallized $Na_{0.44}MnO_2$ with a rod shape (500 nm in width and 5–10 μm in length) as shown in Fig. 5a [5]. A specific capacity of about 140 mAh g^{-1} was obtained at a slow rate (C/200) within the potential range of 2–3.8 V (vs. Na/Na^+), indicating that the reversible insertion/extraction of Na in Na_xMnO_2 occurred with x varying between 0.18 and 0.64. Notably, the evident multi-potential plateaus in charge/discharge curves and multi-peaks in the incremental capacity curves suggest multiple phase transitions occurring during the Na intercalation/deintercalation. In situ X-ray diffraction measurements were carried out to detect the evolution of the multiphases. Six biphasic transition processes were observed during charge and discharge, which were consistent with the numbers of the potential plateaus on the charge/discharge curves. Unfortunately, when the current was increased to 1/10 C, only 80 mAh g^{-1} of capacity was obtained and faded to 50 % over 50 cycles (Fig. 5b). This notable hysteresis in Na intercalation/deintercalation dynamics probably

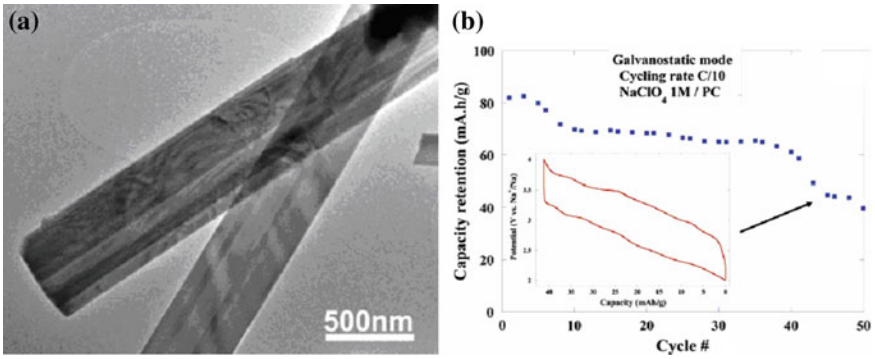

Fig. 5 **a** TEM image showing the rodlike $Na_{0.44}MnO_2$ particles. **b** Capacity retention upon cycling of a $Na_{0.44}MnO_2$/C composite electrode at a C/10 rate [5]

resulted from its large diameter. Hence, a solution should be downsizing the particle of materials to shorten the diffusion path of Na ions.

Recently, Cao et al. reported the electrochemical properties of $Na_{0.44}MnO_2$ nanowires prepared by a polymer–pyrolysis method [4]. The $Na_{0.44}MnO_2$ sample treated at 750 °C was highly crystallized and showed quite uniform nanowire morphology (~50 nm in diameter) (Fig. 6a). The material delivered a reversible capacity of 128 mAh g^{-1} at 1/10 C and exhibited excellent cyclability (77 % capacity retention over 1,000 cycles at 0.5 C), showing great enhancement in the electrochemical performance than previous works [5]. The improvement was considered to be attributed to the high crystallinity and uniform nanowire structure, which can provide a mechanically stable structure as well as a short diffusion path for Na-ion insertion/extraction. An Na-ion full cell was tried by using $Na_{0.44}MnO_2$ as cathode and pyrolyzed carbon as anode. The full cell showed steep charge and discharge curves with an average discharge voltage of 2.7 V and 73 % capacity retention after 100 cycles (Fig. 7).

3.1.3 $Na_xV_yO_z$

Vanadium oxides have variable valences and open formwork structure, which are more suitably used as ion insertion hosts. In the late 1980s, the electrochemical Na-ion interaction behaviors of three types of vanadium oxides were investigated: β–$Na_xV_2O_5$ with channel structure, $Na_{1+x}V_3O_8$ and α–V_2O_5 with layered structure [13]. The reversible Na accommodation levels were ~1.7 mole of Na per mole of α–V_2O_5, ~1.2 mole of Na per mole of β–$Na_{0.33}V_2O_5$ and ~1.6 mole of Na per mole of $Na_{1+x}V_3O_8$ in the potential window of 1.0–3.6 V. Later, Bach et al. studied the electrochemical Na intercalation behaviors of β–$Na_{0.33}V_2O_5$ prepared by two procedures [14, 15]. It showed that β–$Na_{0.33}V_2O_5$ prepared by the sol–gel process can deliver reversibly ~0.7 mole of Na per mole of $Na_{0.33}V_2O_5$ (corresponding to 100 mAh g^{-1}) in the potential window of 2.0–3.4 V, while that prepared by the

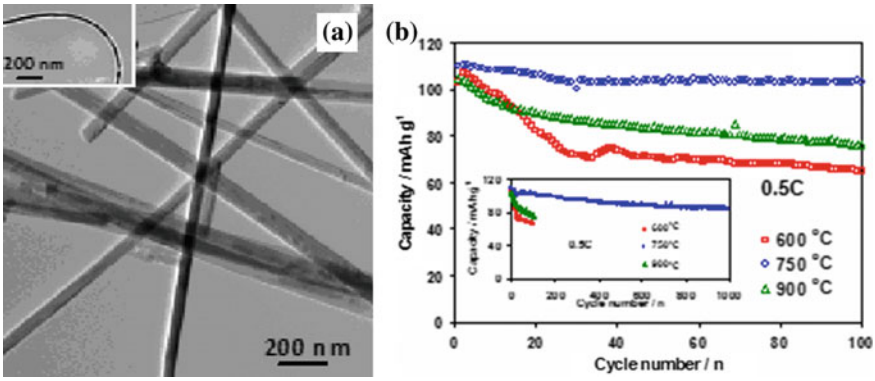

Fig. 6 **a** TEM images of $Na_4Mn_9O_{18}$ nanowires calcined at 750 °C. **b** Cycle performance of $Na_4Mn_9O_{18}$ samples calcined at 600, 750, and 900 °C at a current density of 60 mA g^{-1} (0.5C) [4]

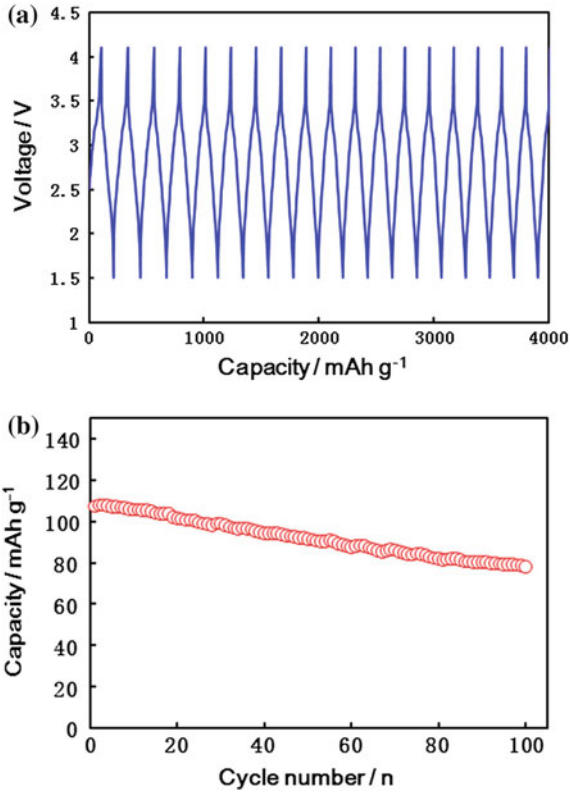

Fig. 7 The charge/discharge profile (**a**) and cycle performance (**b**) of the $Na_4Mn_9O_{18}$/pyrolyzed carbon Na–ion battery in the potential range of 1.5–4.1 V from the second cycle at a constant current of 50 mA g^{-1} (~0.5 C) [4]

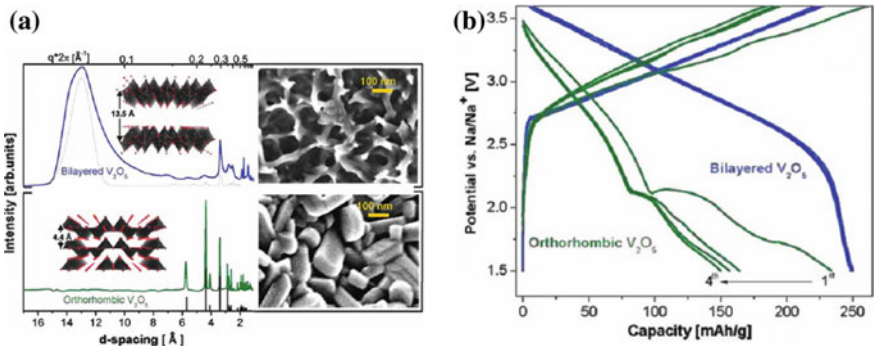

Fig. 8 **a** Synchrotron X-ray diffraction, scanning electron microscopy, and molecular simulations of electrodeposited vanadium oxide: **a** bilayered V_2O_5 annealed in vacuum at 120 °C (*blue*); **b** orthorhombic V_2O_5 annealed in oxygen at 500 °C (*green*). **b** First four charge/discharge cycles of bilayered V_2O_5 and orthorhombic V_2O_5 electrodes. Both cells were cycled at 20 mA g^{-1}, within the potential window of 3.8–1.5 V (vs. Na/Na^+) from 1 M $NaClO_4$ in PC solution [16]

solid-state reaction method can only accommodate 0.17 mole of Na (~20 mAh g^{-1}). The better performance of the material prepared by the sol–gel process probably resulted from its high electrical conductivity along the b-axis, high structural anisotropy and small particular size, which is favorable to fast electronic and ionic diffusion [15]. V_2O_5 with a bilayered structure and an orthorhombic nanostructure were investigated [16]. XRD results showed that the bilayered V_2O_5 is composed of a stacking of V_2O_5 bilayers based on the square–pyramidal VO_5 units arranged in parallel (Fig. 8a). The spacing distance of the bilayers is approximately 13.5 Å, significantly larger than that (only 4.4 Å) of the orthorhombic V_2O_5. Undoubtedly, the larger spacing would be more flexible to accommodate the volume change due to the intercalation of Na ions. As shown in Fig. 8b, the bilayered V_2O_5 electrode delivered a reversible capacity of 250 mAh g^{-1} at 20 mA g^{-1}, higher than that (only 150 mAh g^{-1}) of the orthorhombic V_2O_5. Besides, the bilayered V_2O_5 electrode demonstrated higher average discharge potential and reversible capacity on repeated cycling than its orthorhombic counterpart. This investigation illustrated that tailoring the nanoarchitecture of the materials can offer special functional properties to facilitate the reversible insertion of Na ions.

Analogous to Na_xCoO_2 and Na_xMnO_2, Na_xVO_2 also has different lamellar structure depending on the concentration of Na. The lamellar structure is composed of VO_6 octahedra sharing edges to form VO_2 layers, which are stacked to form O3 and P2-type structures according to the occupation sites of Na ions (octahedral site (O3) for $x = 1$ and trigonal prismatic site (P2) for $x = 0.7$) (Fig. 3a, b). The electrochemical behaviors of O3–$NaVO_2$ and P2–$Na_{0.7}VO_2$ have been studied [17]. Both electrodes exhibited similar charge/discharge profiles (Fig. 9). The intercalation concentration of Na ion for both materials is up to at least 0.5 mol of Na^+ per mole of $NaVO_2$, corresponding to a reversible capacity of

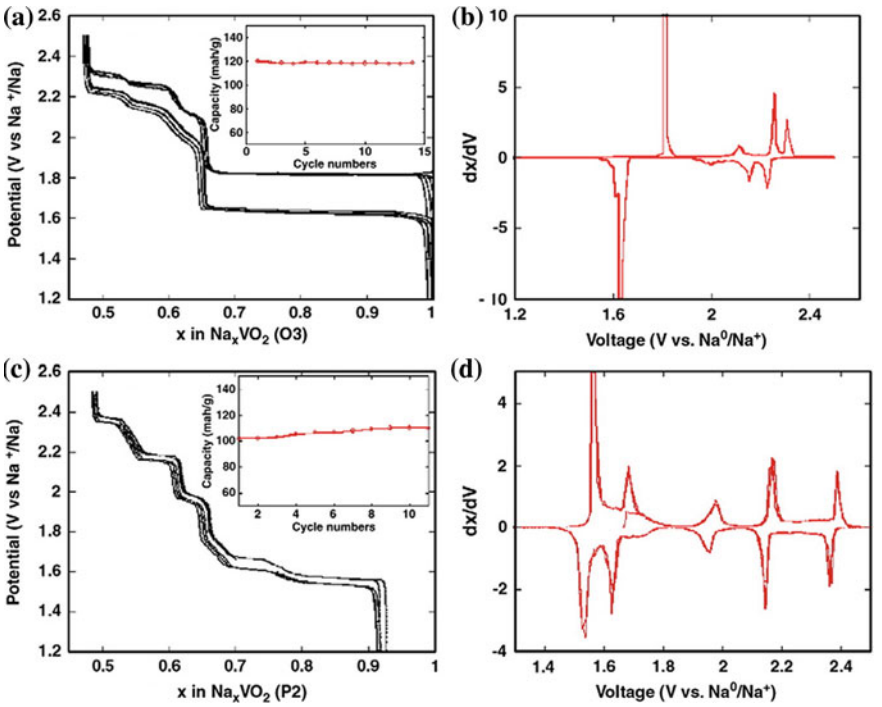

Fig. 9 Voltage–composition curves for **a** $NaVO_2$ (O3) c $Na_{0.7}VO_2$(P2) and associated respectively **b** and **d** derivative curves. Insets indicate the capacity evolution versus number of cycles. The cells using 5–6 mg of positive electrode composites were cycled at C/20. The small polarization between charge and discharge for the P2 phase suggests a high rate capability. This was confirmed by power rate measurements (e.g. signature curves) as this electrode can deliver 90 % of its capacity at 1 C rate [17]

about 130 mAh g^{-1}. For both materials, multiple step phase transitions can be easily observed on the charge/discharge curves and the derivative curves (Fig. 9). A careful observation can find that at low potential range, the voltage variation is about 200 mV for O3–$NaVO_2$, compared to 50 mV for P2–$Na_{0.7}VO_2$. The large difference probably due to O3–$NaVO_2$ is electron insulative, while P2–$Na_{0.7}VO_2$ is semiconductive [18, 19].

3.1.4 Mixed Metal Oxide

Except for Na_xMO_2, mixed metal oxides have also been surveyed in consideration of the combination of the respective properties of different elements. Carlier et al. used Mn to partly replace Co in P2–$Na_{0.67}CoO_2$ to form P2–$Na_{0.67}Co_{0.67}Mn_{0.33}O_2$ based on the consideration of the stabilization of Mn^{4+} ions in the lattice [20]. The charge/discharge curves of the P2–$Na_{0.67}Co_{0.67}Mn_{0.33}O_2$ electrode are shown in

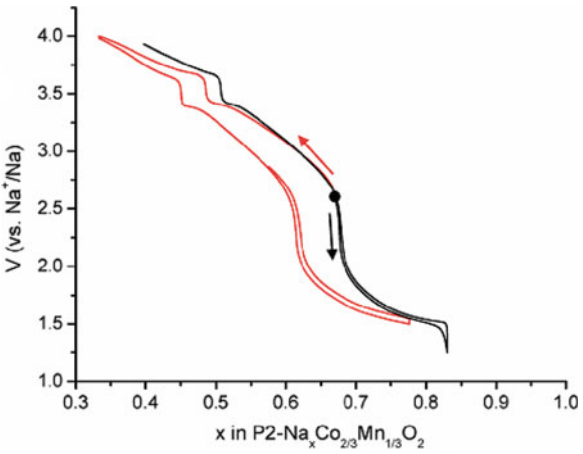

Fig. 10 Cycling curves of $Na/Na_xCo_{2/3}Mn_{1/3}O_2$ cells obtained with a C/100 current rate, starting by a charge (*red curve*) or a discharge (*black curve*) [20]

Fig. 10. Unlike the multiple phase transitions of P2–$Na_{0.67}CoO_2$, it only showed a typical solid-solution insertion/extraction process. The P2–$Na_{0.67}Co_{0.67}Mn_{0.33}O_2$ electrode delivered a high reversible capacity of ~130 mAh g^{-1} (more than 0.5 Na per formula unit). However, the prolonged cycling performance of this electrode is not shown in the literature.

It is believed that in $NaNi_xM_{1-x}O_2$, the displacement of Na^+ by Ni^{2+} can hardly happen due to their large difference in ion radius (Na^+: 1.02 Å, Ni^{2+}: 0.69 Å). Thus, for $NaMnO_2$, the part replacement of Mn by Ni could possibly result in an ordered structure. Komaba et al. prepared $NaNi_{0.5}Mn_{0.5}O_2$ via a co-precipitation method [21]. XRD results showed that only 0.4 % of site exchange of Na with Ni was detected, suggesting a stable layered structure and fast Na-ion diffusion pathway. The $NaNi_{0.5}Mn_{0.5}O_2$ electrode demonstrated an initial discharge capacity of 125 mAh g^{-1} in the potential range of 2.2–3.8 V and high cycling capacity of >100 mAh g^{-1} over 20 cycles (Fig. 11), showing better performance than $NaMnO_2$ [22]. However, the successive phase transition still occurred during charge/discharge, capacity loss with cycling. Thus, stoichiometric Li was introduced into the transition metal layer, to form a stabilizing charge ordering state between Ni^{2+} and Mn^{4+}, for example, $Na_{1.0}Li_{0.2}Ni_{0.25}Mn_{0.75}O_\delta$ [23]. Normalized Mn and Ni K-edge x-ray absorption near edge structure (XANES) spectra showed that the presence of Mn and Ni in the $Na_{1.0}Li_{0.2}Ni_{0.25}Mn_{0.75}O_\delta$ are predominantly Mn^{4+} and Ni^{2+}, respectively, resulting in no Jahn–Teller distortion in the structure. The $Na_{1.0}Li_{0.2}Ni_{0.25}Mn_{0.75}O_\delta$ electrode lost only 2 % of its initial capacity over 50 cycles (Fig. 12), exhibiting excellent cycling stability. The shapes of charge/discharge curves suggest a solid-solution insertion/extraction process, different from the multiple phase transitions of $Na_{0.67}Ni_{0.5}Mn_{0.5}O_2$ (Fig. 11). ICP–OES analysis found that after being charged to 4.2 V, less than 5 % of the total Li in $Na_{1.0}Li_{0.2}Ni_{0.25}Mn_{0.75}O_\delta$ was removed from the lattices. These results demonstrated that Li can stabilize the transition metal layer and restrict the phase transition during Na intercalation/deintercalation.

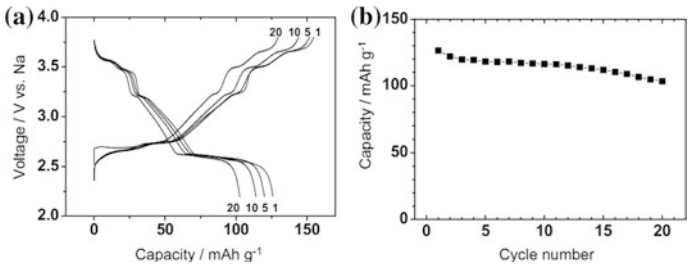

Fig. 11 **a** Galvanostatic charge and discharge curves and **b** variation in discharge capacity of $NaNi_{0.5}Mn_{0.5}O_2$ in Na cells at 4.8 mA g^{-1} [21]

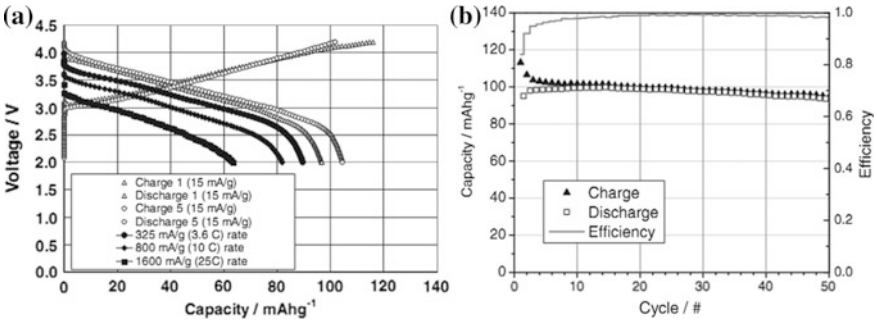

Fig. 12 **a** voltage profiles (first and fifth charge/discharge cycle; open circles and diamonds) for $Na/Na_{0.85}Li_{0.17}Ni_{0.21}Mn_{0.64}O_2$ cell between 4.2 and 2.0 V. Additional discharge voltage profiles for high-rate studies are also shown and labeled in the legend. The trickle charge data points have been removed for clarity, and **b** capacity versus cycle number for $Na/Na_{0.85}Li_{0.17}Ni_{0.21}Mn_{0.64}O_2$ cell between 4.2 and 2.0 V [23]

Recently, Komaba et al. used Fe to substitute Ni in $Na_{0.67}Ni_{0.5}Mn_{0.5}O_2$ to obtain P2–$Na_{0.67}Fe_{0.5}Mn_{0.5}O_2$ [24]. This material achieved a reversible capacity of 190 mAh g^{-1} with an average voltage of 2.75 V (Fig. 13). Hence, the energy density was estimated to be 520 Wh kg^{-1}, which is comparable to that of $LiFePO_4$ (about 530 Wh kg^{-1}) and slightly higher than that of $LiMn_2O_4$ (about 450 Wh kg^{-1}) [24]. If assembled with hard carbon (250–300 mAh g^{-1}) or alloy Sn/Sb (300–500 mAh g^{-1}) anode, the energy density of the system would be hopefully close to that of $LiFePO_4$/C battery, even higher than that of $LiMn_2O_4$/C battery. Besides, this material has the advantage of elemental abundance.

3.2 Polyanion-Based Cathode Materials

Over the last decade, polyanion compounds have attracted much attention as the cathode materials for Li-ion battery, due to their highly thermal and structural

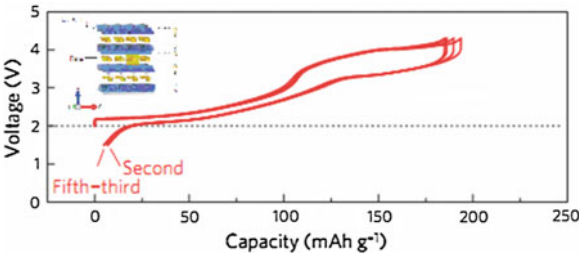

Fig. 13 Galvanostatic charge/discharge (oxidation/reduction) curves for Na/P2–$Na_{0.67}Fe_{0.5}Mn_{0.5}O_2$ cell at a rate of 12 mA/g in the voltage range of 1.5 and 4.3 V [24]

stabilities, such as $LiFePO_4$, $LiMnPO_4$, and so on [25, 26]. Analogously, there are a wide range of Na polyanion compounds with various structures based on the difference in the polyanion and the stoichiometry of the elements. In these compounds, the polyanion polyhedra constitute open 3D frameworks to form ion diffusion channels. Several typical polyanion compounds are illustrated in Fig. 14.

3.2.1 Phosphate Compounds

Among the various Na polyanion compounds, phosphate-based compounds were mostly studied for Na-ion intercalation/deintercalation. NASICON $Na_3V_2(PO_4)_3$, as one of the Na super ion conductors, has fast Na-ion diffusion channels in its crystal structure, [27, 32–34] and hence was widely studied. In the NASICON $Na_3V_2(PO_4)_3$ structure (Fig. 14a), the octahedral VO_6 links the tetrahedral PO_4 via corner to form $[V_2(PO_4)_3]$ unit, which is then interconnected via PO_4 to build up a three-dimensional framework. Na ions selectively occupy two Na sites (Na1 and Na2 in Fig. 14a). One Na ion occupies the Na1 sites, the other two Na ions occupy 2/3 of the Na2 sites. Because the valence of V in $Na_3V_2(PO_4)_3$ is +3, only two Na ions can freely move in/out, corresponding to the redox of the V^{4+}/V^{3+} couple, thus, the theoretical specific capacity of $Na_3V_2(PO_4)_3$ is 117.6 mAh g^{-1}. Uebou et al. first reported the Na intercalation behavior of $Na_3V_2(PO_4)_3$ [35]. In order to improve the electrochemical performance, carbon was used as coating by one-step solid-state reaction [33]. The initial discharge capacity of carbon coated $Na_3V_2(PO_4)_3$ reached 93 mAh g^{-1} with a voltage plateau at 3.4 V and the capacity maintained at 90.9 mAh g^{-1} after 10 cycles in the voltage range of 2.7–3.8 V. Kim et al. synthesized highly crystallized, nano-scaled $Na_3V_2(PO_4)_3$ encapsulated by a conductive carbon-network (Fig. 15a) by using a polyol-assisted pyro-synthetic reaction [32]. The nanophase $Na_3V_2(PO_4)_3$ delivered a capacity of 117 mAh g^{-1} at 0.08 C (Fig. 15b). Balaya et al. reported a porous $Na_3V_2(PO_4)_3$/C composite obtained via a soft template approach [36]. TEM image (Fig. 16a) showed the $Na_3V_2(PO_4)_3$ nanoparticles were well dispersed in the carbon matrix (graphene clusters (SP2 type carbon)). This material not only exhibited a high discharge capacity (116 mAh g^{-1}), but also high rate capability (~65 mAh g^{-1} at 40 C) (Fig. 16b). Moreover, nearly 50 % of the initial capacity was retained after 30,000 cycles at 40 C (Fig. 16c).

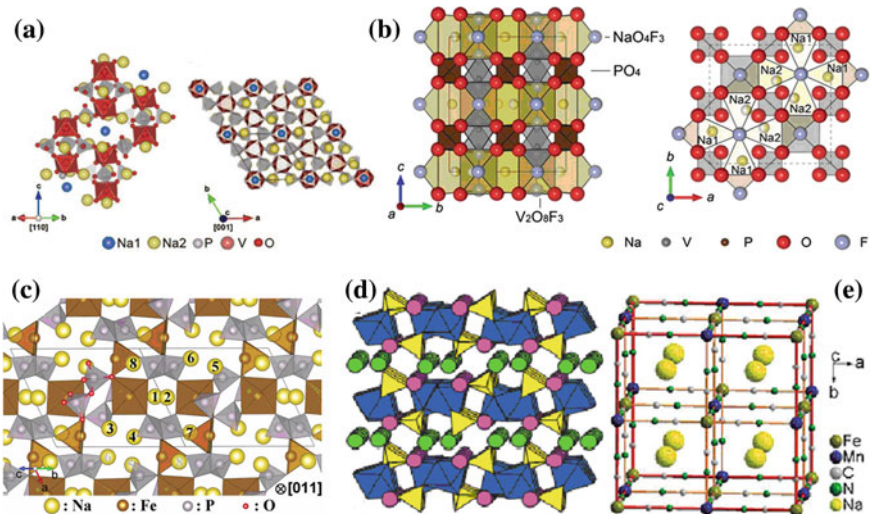

Fig. 14 Crystal structures of some typical polyanion compounds: **a** NASICON–type $Na_3V_2(PO_4)_3$ (R–3c), [27] **b** $Na_3V_2(PO_4)_2F_3$ (P42/mnm), [28] **c** $Na_2FeP_2O_7$ projected along the [011] direction (P1); [29], and **d** Na_2FePO_4F; [30] **e** cubic $NaMnFe(CN)_6$ [31]

Fluorophosphate materials commonly possess higher operating voltages than the corresponding phosphate counterparts [28, 37, 38] due to the strong inductive effect of the fluorine element. $Na_3V_2(PO_4)_2F_3$ (space group of P42/mnm) was first reported by Meins et al. [39]. In the structure, $[V_2O_8F_3]$ bi-octahedral units are linked by the fluorine atoms while the oxygen atoms are all interconnected through the $[PO_4]$ units, leading to the formation of the 3D formwork (Fig. 14b). Na ions have two types of sites in the tunnel: Na1 sites are fully occupied and Na2 sites are half occupied [28]. The charge/discharge profiles of $Na_3V_2(PO_4)_2F_3$ showed two voltage plateaus at about 3.7 and 4.2 V (Fig. 17a), with an average voltage of ~3.95 V [28]. The reversible capacity was ~110 mAh g^{-1} and showed almost no decline after 30 cycles (Fig. 17b). Thus, the energy density of $Na_3V_2(PO_4)_2F_3$ is comparable to that of $LiFePO_4$ and $LiMn_2O_4$ used in Li-ion batteries. Another high-voltage fluorophosphate is $NaVPO_4F$ [37]. Its structure is similar to that of $Na_3Al_2(PO_4)_3F_2$ (space group I4/mmm) [39]. $NaVPO_4F$ was found to have two voltage plateaus at 3.0 and 4.0 V, respectively, and a reversible capacity of ~80 mAh g^{-1} during charge/discharge [28]. This value is much lower than the theoretical capacity (142.5 mAh g^{-1}). Hence, there should still be a very large improvement margin by adopting different synthesis methods or structural tailoring.

A new family with the general formula $Na_3V_2O_{2x}(PO_4)_2F_{3-2x}$ was also studied for high voltage Na intercalation/deintercalation [38]. This type of compounds have similar crystal structure with $Na_3V_2(PO_4)_2F_3$ (tetragonal symmetry, P42/mnm space group) (Fig. 14b). $Na_3V_2O_{2x}(PO_4)_2F_{3-2x}$ showed two voltage plateaus

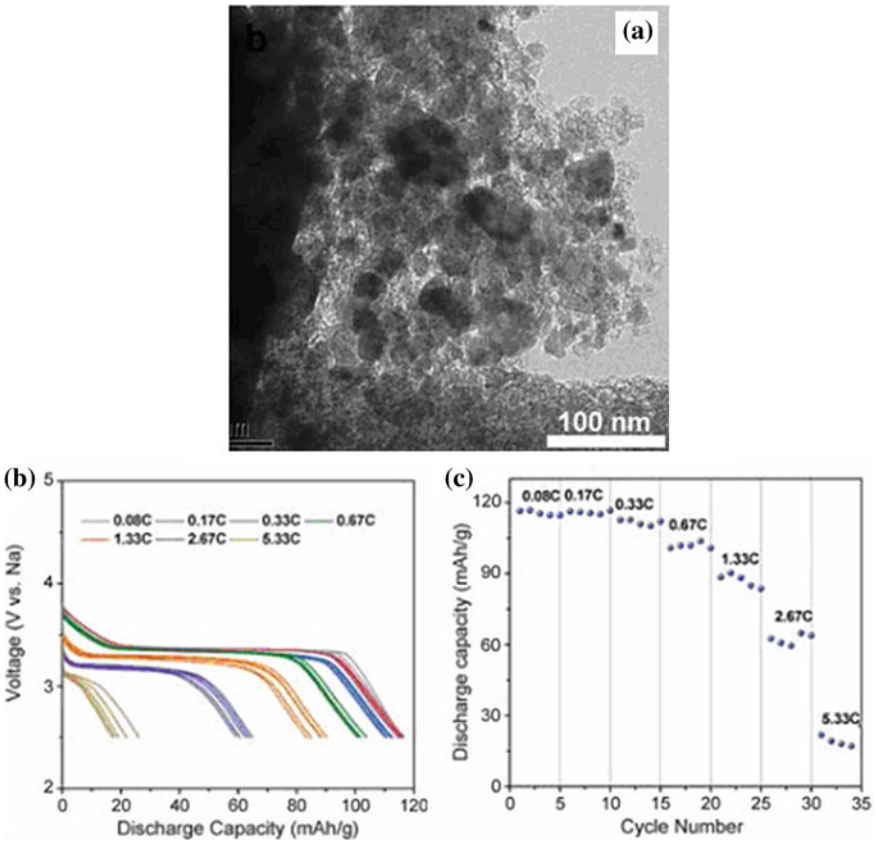

Fig. 15 **a** TEM images of the $Na_3V_2(PO_4)_3$/C prepared by pyro–synthetic reaction. **b** The voltage profiles and **c** the discharge capacities obtained at various C–rates in the voltage range 3.8–2.5 V [32]

at 3.6 and 4.1 V, high rate capability (100 mAh g^{-1} at 1 C) and good cyclability (98 % capacity retention for 30 cycles).

Olivine $LiFePO_4$ has been widely investigated as cathode for Li-ion batteries. Unfortunately, $NaFePO_4$ does not present an olivine phase through conventional high temperature preparation conditions. $NaFePO_4$ usually shows a maricite structure, [40, 41] which is electrochemically inactive [30]. Moreau et al. synthesized olivine $FePO_4$ through chemical oxidation in acetonitrile with NO_2BF_4 [42]. $FePO_4$ is electrochemically active and can allow reversible Na-ion intercalation/deintercalation. In order to obtain electrochemically active olivine-type phosphate compound, Nazar et al. prepared metastable $Na[Mn_{1-x}Fe_x]PO_4$ nanorods by a low-temperature solid-state method [41]. This material showed a sloping voltage profile, indicating a single-phase reaction, which was different from the two-phase reaction of olivine $LiFePO_4$ [25].

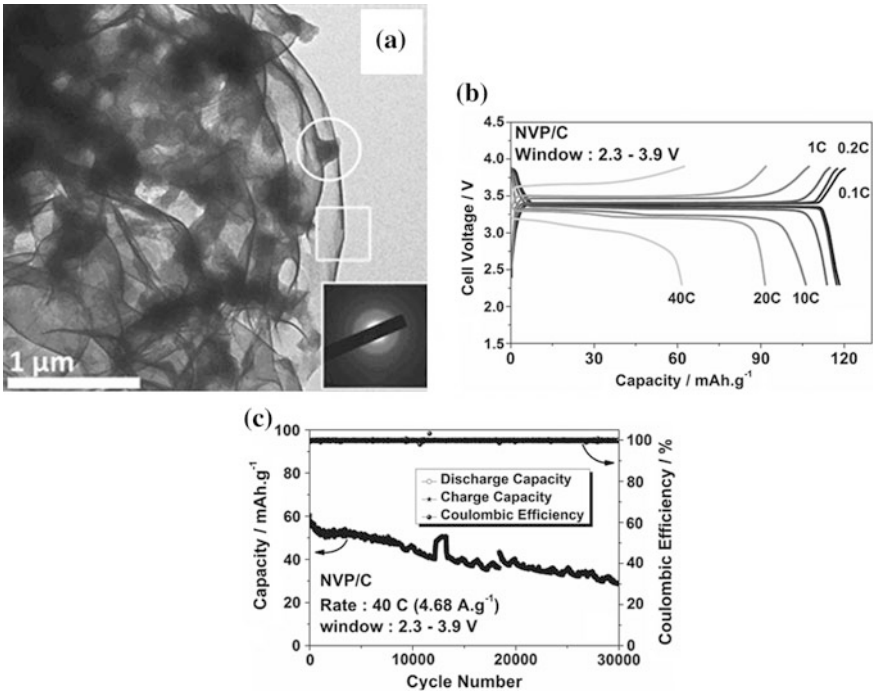

Fig. 16 **a** TEM images of the $Na_3V_2(PO_4)_3$ (NVP) particles anchored on the carbon matrix. **b** Galvanostatic cycling profiles of NVP/C at different current rates between 2.3 and 3.9 V. **c** Long term cycle life and coulombic efficiency for 30,000 cycles at 40 C [36]

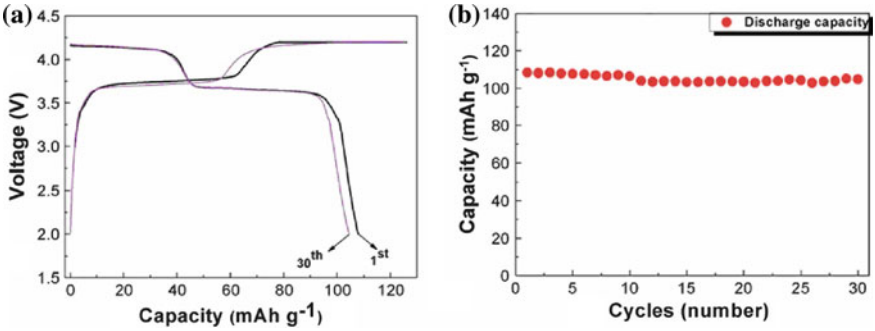

Fig. 17 Electrochemical performance of $Na_3V_2(PO_4)_2F_3$. **a** Charge/discharge profile at the first cycle and thirtieth cycle and **b** cycle performance under a C/10 rate [28]

It was found that $Na_2FeP_2O_7$ was electrochemically active [29]. $Na_2FeP_2O_7$ has a triclinic structure with the space group P1 (Fig. 14c). In the structure, metal polyhedra (FeO_6 and FeO_5) and pyrophosphate (P_2O_7) are interconnected with sharing corners that create various channel structures for Na-ion migration.

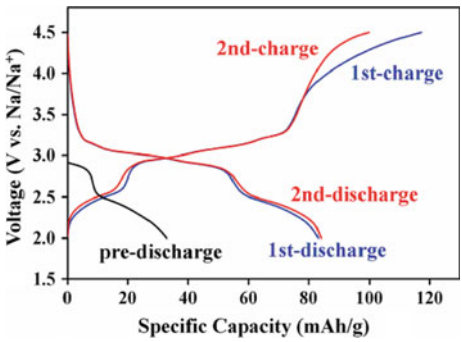

Fig. 18 The voltage profiles of the $Na_2FeP_2O_7$ electrode charged/discharged at a C/20 rate [29]

The charge/discharge curves show one voltage plateau at 2.5 V based on a single-phase reaction and another voltage slope in the potential range of 3.0–3.25 V based on a two-phase reaction (Fig. 18). The material can deliver a reversible capacity of 90 mAh g^{-1} and has good cycling stability, which make it a promising cathode candidate for low cost and long-term Na-ion batteries.

Fe-based mixed polyanion cathode material ($Na_4Fe_3(PO_4)_2(P_2O_7)$) was studied [43]. As shown in Fig. 19, this material exhibits higher reversible capacity (>100 mAh g^{-1}) and potential plateau (~3.0 V) than $Na_2FeP_2O_7$ [29]. $(PO_4F)^{4-}$ based Na–Fe compounds were also investigated [44–46]. Orthorhombic Na_2FePO_4F is composed of $[FePO_4F]$ layers, which are formed by the joining of bioctahedral $Fe_2O_7F_2$ units with PO_4 tetrahedra. The $[FePO_4F]$ layers are stacked to form two-dimensional pathways providing Na-ion migration. The reversible Na-ion intercalation/deintercalation capacity reached 120 mAh g^{-1}, with an average voltage of 3.0 V and good cycling stability [44]. If Fe was partly substituted by Mn, the electrochemical performance of this material decreased rapidly with increasing Mn content, due to a strong tendency of structural transition from 2D to 3D [44].

3.2.2 Hexacyano-Type Compound

In the above-mentioned cathode materials, Na ions lie in the complex environment composed of oxides and polyanions. The immigration of Na ions in these close packed structures is difficult due to the strong interaction between Na^+ and O^{2-} ions. The replacement of O^{2-} ions by CN^- ions would greatly weaken the interaction of the complexants with Na^+, leading to the reduction of the activation energy for Na^+ ion migration. Thus, Hexacyano-type compounds have attracted great attention [31, 47, 48].

Yang et al. proposed a new family of Na transition metal cyanides, such as hexacyanoferrate $Na_4Fe(CN)_6$ and Prussian blue $Na_xM_yFe(CN)_6$ as Na-ion hosts. The as prepared $Na_4Fe(CN)_6$/C nanocomposite displayed a full utilization of its redox capacity of 87 mAh g^{-1} at a high potential of ~3.4 V, an excellent cycling

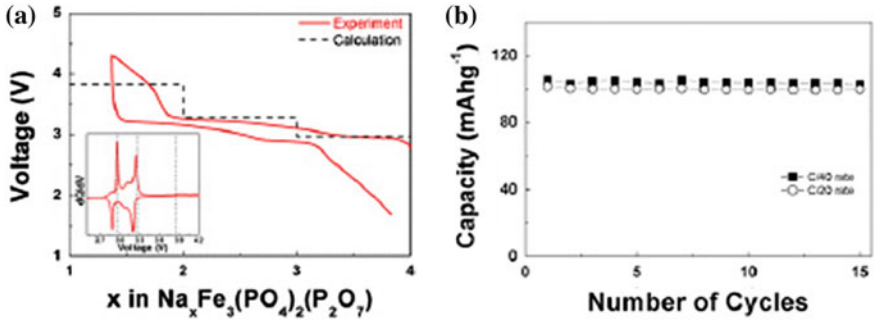

Fig. 19 **a** Galvanostatic charge/discharge profiles of $Na_4Fe_3(PO_4)_2(P_2O_7)$ under a C/40 rate and the calculated average voltage at each region. The inset shows the dQ/dV curve of the initial charge/discharge profile. **b** Cycle performance of a Na cell under C/40 and C/20 rates [43]

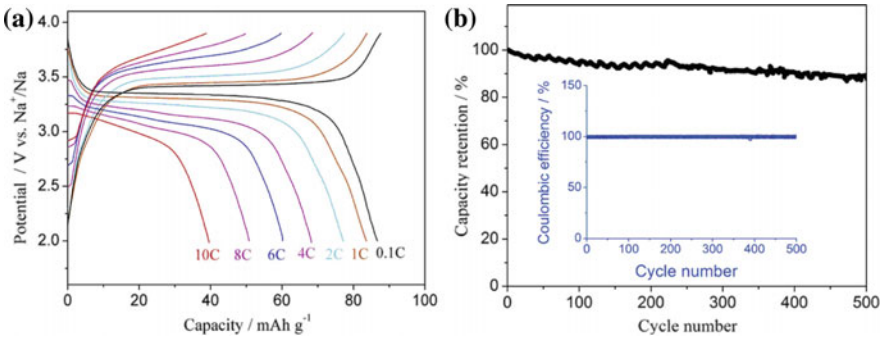

Fig. 20 Electrochemical characterizations of the $Na_4Fe(CN)_6$/C composite: **a** charge and discharge profiles at various C rates (1C = 90 mA g^{-1}); and **b** discharge capacity versus cycle numbers [48]

stability with 88 % capacity retention over 500 cycles and superior high rate capability with 45 % capacity delivery at a 10 C rate (Fig. 20) [48]. Prussian blue $Na_xM_yFe(CN)_6$ (M = Fe, Co, Ni, Mn) compounds showed very different electrochemical behaviors, when M was Fe, Co, and Mn, the specific capacities of $Na_xFe_yFe(CN)_6$, $Na_xCo_yFe(CN)_6$, and $Na_xMn_yFe(CN)_6$ reached 113, 120, and 113 mAh g^{-1}, respectively, indicating that both the $Fe(CN)_6^{4-}$ and M^{2+} ions in the Prussian blue lattices were electrochemically active. When M was Ni, Ni ions in the Prussian blue lattice were found to be electrochemically inactive and $Na_xNi_yFe(CN)_6$ could only deliver a specific capacity of 64 mAh g^{-1} but with quite stable cyclability [31, 47]. Goodenough et al. reported two types of Na manganese hexacyanoferrates: cubic $Na_{1.40}MnFe(CN)_6$ and rhombohedral $Na_{1.72}MnFe(CN)_6$ [31]. The rhombohedral $Na_{1.72}MnFe(CN)_6$ (Fig. 14e) showed higher discharge capacity of 130 mAh g^{-1} while the cubic $Na_{1.40}MnFe(CN)_6$ exhibited higher capacity retention of 96 % after 30 cycles. Overall, Hexacyano-type compounds

with open framework have shown several advantages as Na-ion host materials: (1) high discharge voltage plateau; (2) excellent cycling stability due to their stable frameworks during Na intercalation/deintercalation; (3) high reversible capacity (>120 mAh g^{-1}); (4) abundant resources and low cost. So, Hexacyano-type compounds should be promising candidates as cathode hosts for low-cost and long-term Na-ion batteries.

4 Anode Materials for Na-Ion Batteries

Appropriate anode materials should meet the following requirements:

1. Na-ion intercalation/deintercalation potentials are close to Na/Na^+, and less influenced by the concentration of Na ions in the lattices, so as to guarantee high output voltage in the full cells.
2. The reversible Na-ion intercalation capacity and the discharge/charge efficiency are as high as possible to provide high capacity density.
3. Low volume change during Na-ion intercalation/deintercalation, good compatibility with electrolyte to obtain good cycling stability.
4. High chemical as well as thermal stability to ensure intrinsical safety.
5. High electron conductivity and Na-ion diffusion rate to offer high C rate at charge/discharge.
6. Low cost, abundant resources, environmental benignity, and easy to mass produce.

The possible anode materials for Na-ion batteries mainly include carbonaceous materials, alloy, and some metal oxides.

4.1 Carbonaceous Materials

Graphite and graphite-like materials were most often surveyed for alkali-ion intercalation anodes. The Na intercalation behavior in graphite was first investigated in the late 1970s [49, 50–52]. However, the intercalation amount of Na in graphite is low (~NaC_{64}) compared to that of LiC_6 and KC_8. Other carbon material with microcrystalline graphitic structure and microporous domains were found to have high Na storage capacity, such as carbon black (121 mAh g^{-1}), [53] petroleum coke, [51] and carbon fibers (209 mAh g^{-1}) [52, 54, 55].

A variety of precursors were used to obtain different structured hard carbon materials. Dahn et al. found that the hard carbon obtained by the glucose pyrolyzation showed reversible Na intercalation capacity of ~300 mAh g^{-1} [56]. Microspherical hard carbon particles with disordered nanostructure (Fig. 21a) synthesized by pyrolyzing resorcinol–formaldehyde compounds, [57] delivered an initial capacity of 285 mAh g^{-1}, and over 255 mAh g^{-1} after seven cycles in

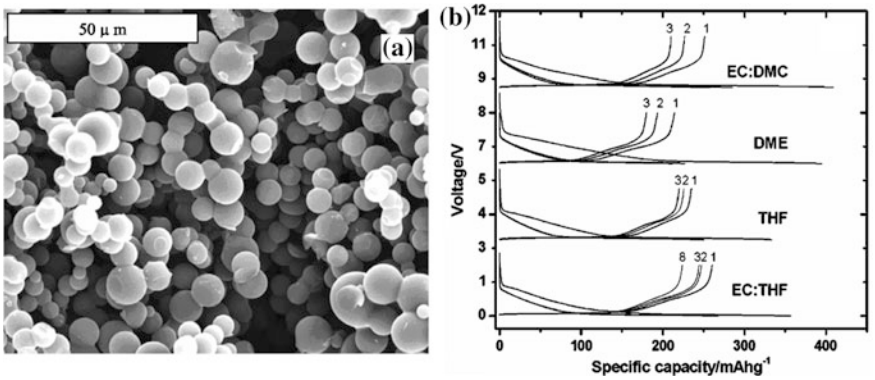

Fig. 21 SEM of carbon microspheres. **b** Voltage/capacity plots corresponding to the first discharge/charge cycles of carbon aerogel microspheres in Na cells, 1 M $NaClO_4$ dissolved in different solutions as electrolyte [57]

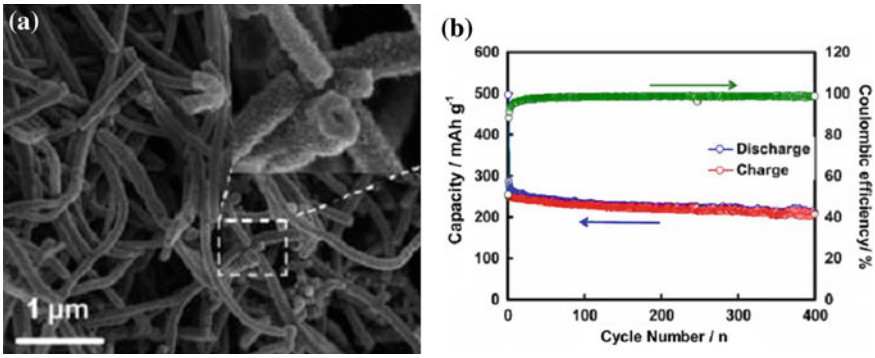

Fig. 22 **a** SEM images of the PANI–HNWs. **b** Cycle performance of the HCNW electrode at a current density of 50 mA/g (0.2 C) [58]

EC–THF mixture electrolyte (Fig. 21 b). Cao et al. reported hollow carbon nanowires (HCNWs) prepared by the pyrolyzation of a hollow polyaniline nanowire precursor (Fig. 22a) [58]. The HCNW electrode delivered high reversible capacity of 251 mAh g^{-1} and excellent cycling stability (82.2 % of capacity retention over 400 cycles) (Fig. 22b). Such excellent electrochemical performance was ascribed to the HCNWs that had a uniform hollow nanowire structure and an appropriate interlayer distance, leading to short diffusion distance for Na insertion, stable material structure, and feasible approach for Na-ion insertion into carbon layers. Besides, Komaba et al. reported the effect of electrolytes on Na insertion behavior in hard carbon [59]. It was found that in EC:DEC(1:1) solution containing 1 mol L^{-1} $NaClO_4$, the hard carbon electrode exhibited a high capacity of ca. 240 mAh g^{-1} with a stable capacity retention over 100 cycles. This was related

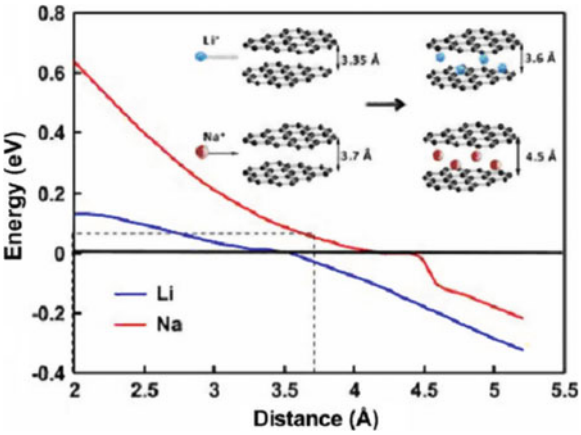

Fig. 23 Theoretical energy cost for Na (*red curve*) and Li (*blue curve*) ions insertion into carbon as a function of carbon interlayer distance [58]

to the different chemical and electrochemical reaction of carbonate solution on the surface of the hard carbon material [59].

It was found that the charge/discharge profiles of the hard carbon anodes commonly comprise two parts: a slope at the high potential region and a plateau at the low potential region, as shown in Fig. 21b [56, 59]. Several spectroscopy technologies have been used to investigate the specific mechanism, such as ex-situ or in-situ X-ray diffraction, small-angle X-ray scattering (SAXS), [55, 60, 61] ^{23}Na magic angle spinning nuclear magnetic resonance (MAS NMR) spectra, [57] and Raman spectroscopy [59]. By in-situ SAXS investigation, Dahn et al. first demonstrated that the slope at high potential region corresponded to Na intercalation/deintercalation between the graphene layers and the plateau at the low potential region corresponded to Na adsorption/desorption in the nanopores of the carbon particles [60]. ^{23}Na MAS NMR spectra corresponding to the hard carbon microspheres also clearly showed that two signal responses during charge and discharge, which could be ascribed to Na insertion between misaligned graphene carbon framework and in the nanocavities or on a surface solid film, respectively [57]. In Raman spectroscopy, the shift of the G-band indicates the change of the state of negatively charged graphenes, the redshift observed during the voltage-sloping region corresponds to the Na insertion between the graphene layers. No shift of G-band in lower potential region can be ascribed to the formation of a nano-sized cluster of quasimetallic Na in the nanopores of the hard carbon [59].

It is obvious that the interplanar distances of the graphene layers in hard carbon will play a vital role on the Na intercalation behavior. Cao et al. carried out a theoretical simulation on the energy cost for the Na-ion insertion into carbon as a function of the carbon interlayer distance (Fig. 23) [58]. For comparison, the energy cost curve for Li-ion insertion into carbon was also calculated (Fig. 23). For graphite with an interlayer spacing of 0.335 nm, the energy cost for Li-ion and Na-ion insertion are 0.03 and 0.12 eV, respectively. In consideration that the energy of the thermal fluctuations at room temperature is 0.00257 eV, Li-ion intercalation into graphite layers is permissible while Na-ion is prohibitive.

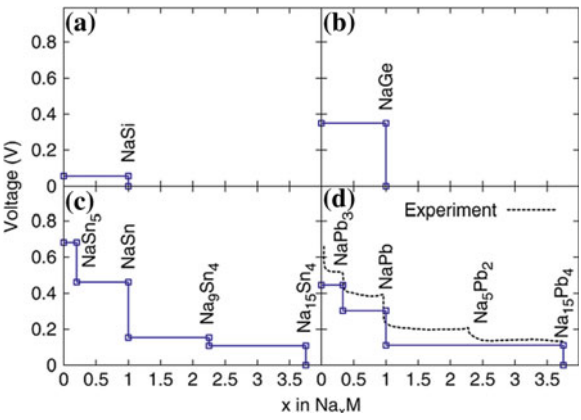

Fig. 24 Na–M voltage curves calculated using DFT and known Na–M crystal structures. **a** M–Si **b** M–Ge **c** M–Sn, and **d** M–Pb [63]

However, when the layer spacings increase to 0.37 nm, the energy barrier for Na-ion insertion drops markedly to 0.053 eV, indicating a feasibility of Na-ion insertion. Therefore, it is important to seek carbon materials with appropriate layer spacing to improve the Na insertion performance.

4.2 Alloy Materials

As shown above, the Na storage capacity of carbonaceous materials is commonly <300 mAh g^{-1}, it is difficult to further enhance their capacity due to the limited host sites in the carbon structure. Besides, the Na intercalation potentials in carbonaceous materials are close to the plating potential of Na ions, which would lead to a safety concern. Hence, it is necessary to seek alternative anode materials for high-capacity and high-safety Na-ion batteries. Analogous to Li alloy, Na can also alloy with some Group IVA and VA metal elements, such as Sn, Sb, Pb, and Ge [62]. These alloys are estimated to deliver high reversible capacity due to their high theoretical-specific capacities, such as 847 ($Na_{15}Sn_4$), 660 (Na_3Sb), 1108 (Na_3Ge), and 484 ($Na_{15}Pb_4$) mAh g^{-1}, respectively. Besides, the alloying reactions have higher thermodynamic potential than Na–C reactions, making them potentially safer. Recently, Ceder et al. reported the Na–M voltage curves calculated through density functional theory (DFT) for Si, Ge, Sn, and Pb (Fig. 24) [63]. The voltage curves for Si and Ge showed only one voltage plateau, indicating the formation of a single alloy phase. On the contrary, the voltage curves for Sn and Pb exhibited multi-voltage plateaus, corresponding to the formation of multiple alloy phases during the Na intercalation/deintercalation. These theoretical calculations are in good agreement with the experimental data in the literatures [62, 64–68] Jow et al. studied the electrochemical performance of $Na_{15}Pb_4$ alloy for Na intercalation [64]. The metallurgically formed $Na_{15}Pb_4$ gave out 86 % of the Na storage capacity at a low rate of 50 μA cm^{-3}.

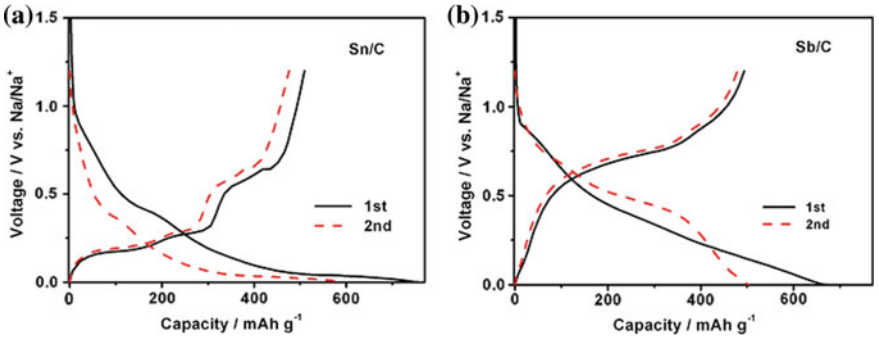

Fig. 25 The initial two discharge/charge profiles of the **a** Sn/C and **b** Sb/C nanocomposite electrodes between 0.0 and 1.2 V versus Na/Na^+ at a current rate of 100 mA g^{-1} [62]

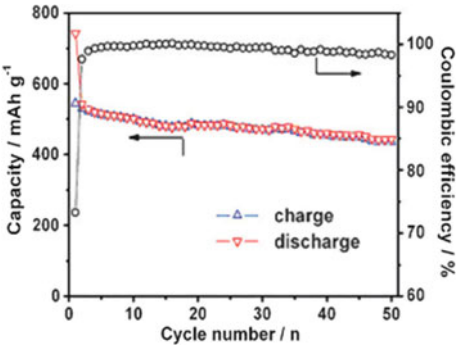

Fig. 26 Cycling performance of the SnSb/C nanocomposite electrode at a cycling rate of 100 mA g^{-1} [62]

Xiao et al. first studied the Na storage properties in Sn and Sb (Fig. 25) [62]. As shown in Fig. 25a, the voltage profiles of Sn/C nanocomposites clearly showed two discharge and four charge plateaus, reflecting the stepwise Na–Sn alloy phase transition processes, similar to the calculated theoretical data (Fig. 24). The Sn/C electrode delivered a high reversible capacity of 509 mAh g^{-1} (Fig. 25a). After deducting the capacity associated with carbon black, Sn individually can offer a capacity of 653 mAh g^{-1}, which is about 77.1 % of the theoretical capacity of 847 mAh g^{-1} based on $Na_{15}Sn_4$. The Sb/C electrode also showed high initial capacity of 494 mAh g^{-1} (Fig. 25b). Sb individually can offer a capacity of 631 mAh g^{-1}, which is equivalent to 95.6 % of the theoretical capacity based on Na_3Sb (660 mAh g^{-1}). But both electrodes exhibited a rapid decrease in capacity with cycling [62]. This situation is commonly found in Li–alloy electrode, resulting from severe volume changes of the electrode during the alloying/dealloying processes which cause the pulverization of the metal particles, the loss of the electric conducting between the active materials. However, the SnSb/C composite exhibited high reversible capacity of 544 mAh g^{-1} and particularly excellent cycling capability with 80 % of capacity retention over 50 cycles (Fig. 26) [62]. It is proposed that when discharged to 0.4 V, Na ions insert into the SnSb

alloy to form Na_3Sb and Sn phase, while the Sn phase is inactive at this time and acts as the conducting buffer to maintain structural integrity. When discharge continues to <0.4 V, alloying reaction of Na with Sn occurs and Na_3Sb is inactive and serves as a buffer matrix. So, such a self-supporting network can maintain the integrity and conductivity of the whole electrode material to provide good cycling stability of the electrode.

Yang et al. prepared an Sb/C composite by mechanical milling, which was composed of ~10 nm nanocrystallite Sb embedded in the carbon matrix [67]. The naocrystalline Sb/C electrode delivered an initial capacity as high as 610 mAh g^{-1} based on the pure Sb, very close to the theoretical capacity (Na_3Sb, 660 mAh g^{-1}). The Sb/C electrode in a 5 % FEC-containing electrolyte maintained an almost constant capacity of 575 mAh g^{-1} over 100 cycles [67]. The excellent electrochemical performances enable the Sb/C nanocomposite to be used as candidate anode for high capacity and high safety Na-ion batteries.

4.3 Metal Oxide Materials

In general, the Na storage capacities in materials with an intercalation reaction mechanism are limited by the number of host sites in their structures. One way to circumvent this intrinsic limitation and to achieve higher capacities would be the use of materials with a reversible conversion reaction mechanism. The Na storage capacity then depends on the change of the redox valence states of the material while not the material structure. Such materials are mainly oxides, [69–71] fluorides, [72] and sulfides [73]. Among them, oxides have the most appropriate Na storage potentials. Tirado et al. first reported the electrochemical characteristics of $NiCo_2O_4$ spinel for Na storage [70]. It showed that the $NiCo_2O_4$ electrode delivered a reversible capacity of ca. 200 mAh g^{-1} with an average potential of 1.5 V. Co_3O_4 was also investigated as Na storage anode [71]. This material delivered a reversible capacity of 444 mAh g^{-1}, but with poor cycling performance.

Johnson et al. synthesized amorphous titanium dioxide nanotube (TiO_2 NT) to investigate its utilization for Na-ion batteries [74]. It was found that only when the size of the nanotubes increased to >80 nm (wall thickness >15 nm), the amorphous TiO_2 could show relatively low specific capacity initially, which then self-improved as cycling proceeded. The electrode delivered a reversible capacity of 75 mAh g^{-1} in the first cycle and the capacity increased to 150 mAh g^{-1} after 15 cycles (Fig. 27a). This behavior can be explained that Na ions cannot adsorb on TiO_2 surface and screen the charge of electrons injected into the TiO_2 matrix in the relatively small-diameter tube, so that insufficient Na ions can not establish critical ion concentration that supports cycling. Thus, it is important to tailor the nanostructure of materials to enhance their Na insertion performance. Palacin et al. reported the use of $Na_2Ti_3O_7$ as anode for Na-ion batteries [75, 76]. $Na_2Ti_3O_7$

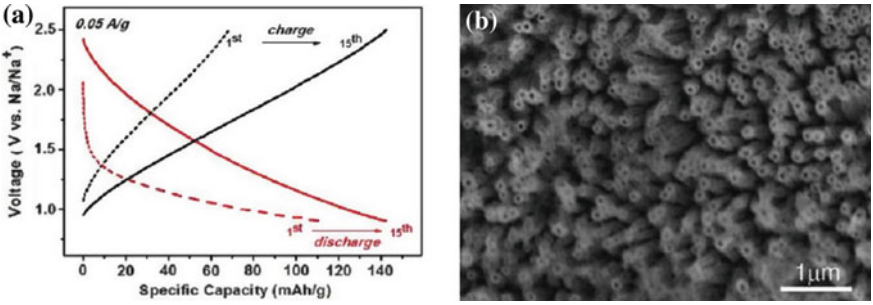

Fig. 27 **a** Charge/discharge galvanostatic curves of amorphous 80 nm I.D. TiO_2 NT in Na half cell (*red* for discharge and *black* for charge) cycled between 2.5 and 0.9 V versus Na/Na^+ at 0.05A g^{-1}. **b** SEM top–view images of TiO_2 NT electrodes [74]

consists of zigzag layers of Ti–O octahedra with Na ions in the interlayer spacing [77]. Additional Na ions (2 Na ions per formular unit) can insert into the interlayer space. The $Na_2Ti_3O_7$ electrode could reversibly deliver a capacity of 200 mAh g^{-1} at an average potential of 0.3 V and with good cycling stability.

5 Summary and Outlook

Although along with the development of Li intercalation materials, their Na analogs have also been investigated, the performance of Na intercalation materials is far inferior to the lithium counterparts, the energy density of the thus constructed Na-ion batteries then is far below that of Li-ion batteries. Moreover, some research on Na intercalation reactions focus only on the superficial exploratory study, deep consideration of materials and systems are bare. Time enters in the twenty-first century, and due to the shortage of fossil fuel and the worsening of environmental pollution, the development of renewable energy sources and electric vehicles has drawn more and more attention. Li-ion batteries that have occupied the portable electronic product market are considered as the ideal system for electric vehicle propulsion and renewable electric power storage. However, due to the concern of insufficient Li reserves, scientists again begin to show interest in Na-ion battery systems, which have no resource constraints. In the last 3 years, a wide range of new types of Na intercalation materials have been proposed and deeply investigated. The electrochemical performance of several materials was close to that of Li-ion batteries. For example, P2–$Na_{0.67}Fe_{0.5}Mn_{0.5}O_2$ cathode material can reach an energy density of 520 Wh kg^{-1}, which is comparable to that of $LiFePO_4$ (about 530 Wh kg^{-1}) and slightly higher than $LiMn_2O_4$ (about 450 Wh kg^{-1}). Rhombohedral $Na_{1.72}MnFe(CN)_6$ has a reversible capacity of 134 mAh g^{-1} with a high potential plateau of 3.4 V, very close to that of $LiFePO_4$ (140 mAh g^{-1} and 3.4 V potential plateau). For the anode, hard carbon with hollow nanowire structure can

deliver a reversible capacity of 250 mAh g^{-1} with excellent cycling stability. The capacity of Sb/C nanocomposite can achieve 420 mAh g^{-1} based on the material including Sb and carbon. The electrochemical performance of these anode materials is close or superior to graphite commercially used in Li-ion batteries. If we use the above-mentioned materials to construct practical Na-ion batteries, the energy density of the batteries would be close to the commercial graphite/$LiFePO_4$ system. Although some achievements are obtained in Na intercalation materials, they are still far from realizing the real utility of Na-ion batteries. Some work should be further pursued, such as the industrial mass production of materials, balance and interaction of the cathode and anode, special design of the cell configuration, and safety protection of batteries. All in all, the development of Na-ion batteries is facing great chances as well as challenges, we believe that through the unremitting efforts of scientists, this newly emerging energy storage system will finally realize its application.

References

1. Slater MD, Kim D et al (2013) Sodium-ion batteries. Adv Funct Mater 23:947–958
2. Kim S-W, Seo D-H et al (2012) Electrode materials for rechargeable sodium-ion batteries: potential alternatives to current lithium-ion batteries. Adv Energy Mater 2:710–721
3. Delmas C, Fouassier C et al (1980) Structural classification and properties of the layered oxides. Physica B+C 99:81–85
4. Cao YL, Xiao LF et al (2011) Reversible sodium ion insertion in single crystalline manganese oxide nanowires with long cycle life. Adv Mater 23:3155–3160
5. Sauvage F, Laffont L et al (2007) Study of the insertion/deinsertion mechanism of sodium into $Na_{0.44}MnO_2$. Inorg Chem 46:3289–3294
6. Whitacre JF, Tevar A et al (2010) $Na_4Mn_9O_{18}$ as a positive electrode material for an aqueous electrolyte sodium-ion energy storage device. Electrochem Commun 12:463–466
7. Saint JA, Doeff MM et al (2008) Electrode materials with the $Na_{0.44}MnO_2$ structure: effect of titanium substitution on physical and electrochemical properties. Chem Mater 20:3404–3411
8. Braconnier J-J, Delmas C et al (1980) Comportement electrochimique des phases Na_xCoO_2. Mater Res Bull 15:1797–1804
9. Berthelot R, Carlier D et al (2011) Electrochemical investigation of the P2–Na_xCoO_2 phase diagram. Nat Mater 10:74–80
10. Bhide A, Hariharan K (2011) Physicochemical properties of Na_xCoO_2 as a cathode for solid state sodium battery. Solid State Ionics 192:360–363
11. Parant J-P, Olazcuaga R et al (1971) Sur quelques nouvelles phases de formule Na_xMnO_2 ($x \leq 1$). J Solid State Chem 3:1–11
12. Caballero A, Hernan L et al (2002) Synthesis and characterization of high-temperature hexagonal P2-$Na_{0.6}MnO_2$ and its electrochemical behaviour as cathode in sodium cells. J Mater Chem 12:1142–1147
13. West K, Zachau-Christiansen B et al (1988) Sodium insertion in vanadium oxides. Solid State Ionics 28–30(Part 2):1128–1131
14. Bach S, Baffier N et al (1989) Electrochemical sodium intercalation in $Na_{0.33}V_2O_5$ bronze synthesized by a sol-gel process. Solid State Ionics 37:41–49
15. Pereira-Ramos JP, Messina R et al (1990) Influence of the synthesis via a sol-gel process on the electrochemical lithium and sodium insertion in β-$Na_{0.33}V_2O_5$. Solid State Ionics 40–41(Part 2):970–973

16. Tepavcevic S, Xiong H et al (2012) Nanostructured bilayered vanadium oxide electrodes for rechargeable sodium-ion batteries. ACS Nano 6:530–538
17. Hamani D, Ati M et al (2011) Na_xVO_2 as possible electrode for Na-ion batteries. Electrochem Commun 13:938–941
18. Onoda M (2008) Geometrically frustrated triangular lattice system Na_xVO_2: superparamagnetism in x = 1 and trimerization in x approximate to 0.7. J Phys-Condens Matter 20:145205
19. McQueen TM, Stephens PW et al (2008) Successive Orbital Ordering Transitions in $NaVO_2$. Phys Rev Lett 101:166402
20. Carlier D, Cheng JH et al (2011) The P2-$Na_{2/3}Co_{2/3}Mn_{1/3}O_2$ phase: structure, physical properties and electrochemical behavior as positive electrode in sodium battery. Dalton Trans 40:9306–9312
21. Komaba S, Nakayama T et al (2009) Electrochemically reversible sodium intercalation of layered $NaNi_{0.5}Mn_{0.5}O_2$ and $NaCrO_2$. ECS Trans 16:43–55
22. Mendiboure A, Delmas C et al (1985) Electrochemical intercalation and deintercalation of $NaMnO_2$ bronzes. J Solid State Chem 57:323–331
23. Kim D, Kang SH et al (2011) Enabling sodium batteries using lithium-substituted sodium layered transition metal oxide cathodes. Adv Energy Mater 1:333–336
24. Yabuuchi N, Kajiyama M et al (2012) P2-type $Na_x[Fe_{1/2}Mn_{1/2}]O_2$ made from earth-abundant elements for rechargeable Na batteries. Nat Mater 11:512–517
25. Padhi AK, Nanjundaswamy KS et al (1997) Phospho-olivines as positive-electrode materials for rechargeable lithium batteries. J Electrochem Soc 144:1188–1194
26. Martha SK, Markovsky B et al (2009) $LiMnPO_4$ as an advanced cathode material for rechargeable lithium batteries. J Electrochem Soc 156:A541–A552
27. Lim SY, Kim H et al (2012) Electrochemical and thermal properties of NASICON structured $Na_3V_2(PO_4)_3$ as a sodium rechargeable battery cathode: a combined experimental and theoretical study. J Electrochem Soc 159:A1393–A1397
28. Shakoor RA, Seo DH et al (2012) A combined first principles and experimental study on $Na_3V_2(PO_4)_2F_3$ for rechargeable Na batteries. J Mater Chem 22:20535–20541
29. Kim H, Shakoor RA et al (2013) $Na_2FeP_2O_7$ as a promising iron-based pyrophosphate cathode for sodium rechargeable batteries: a combined experimental and theoretical study. Adv Funct Mater 23:1147–1155
30. Ellis BL, Makahnouk WRM et al (2007) A multifunctional 3.5 V iron-based phosphate cathode for rechargeable batteries. Nat Mater 6:749–753
31. Wang L, Lu Y et al (2013) A superior low-cost cathode for a Na-ion battery. Angew Chem Int Ed 52:1964–1967
32. Kang J, Baek S et al (2012) High rate performance of a $Na_3V_2(PO_4)_3$/C cathode prepared by pyro-synthesis for sodium-ion batteries. J Mater Chem 22:20857–20860
33. Jian Z, Zhao L et al (2012) Carbon coated $Na_3V_2(PO_4)_3$ as novel electrode material for sodium ion batteries. Electrochem Commun 14:86–89
34. Jian Z, Han W et al (2013) Superior electrochemical performance and storage mechanism of $Na_3V_2(PO_4)_3$ cathode for room-temperature sodium-ion batteries. Adv Energy Mater 3:156–160
35. Uebou Y, Kiyabu T et al (2002) The reports of institute of advanced material study (vol 16). Kyushu University, Fukuoka, p 1
36. Saravanan K, Mason CW et al (2013) The first report on excellent cycling stability and superior rate capability of $Na_3V_2(PO_4)_3$ for sodium ion batteries. Adv Energy Mater 3:444–450
37. Barker J, Saidi MY et al (2003) A sodium-ion cell based on the fluorophosphate compound $NaVPO_4F$. Electrochem Solid-State Lett 6:A1–A4
38. Serras P, Palomares V et al (2012) High voltage cathode materials for Na-ion batteries of general formula $Na_3V_2O_{2x}(PO_4)_2F_{3-2x}$. J Mater Chem 22:22301–22308

39. Le Meins JM, Crosnier-Lopez MP et al (1999) Phase Transitions in the $Na_3M_2(PO_4)_2F_3$ Family (M = Al^{3+}, V^{3+}, Cr^{3+}, Fe^{3+}, Ga^{3+}): Synthesis, Thermal, Structural, and Magnetic Studies. J Solid State Chem 148:260–277
40. Zaghib K, Trottier J et al (2011) Characterization of Na-based phosphate as electrode materials for electrochemical cells. J Power Sources 196:9612–9617
41. Lee KT, Ramesh TN et al (2011) Topochemical synthesis of sodium metal phosphate olivines for sodium-ion batteries. Chem Mater 23:3593–3600
42. Moreau P, Guyomard D et al (2010) Structure and stability of sodium intercalated phases in olivine $FePO_4$. Chem Mater 22:4126–4128
43. Kim H, Park I et al (2012) New iron-based mixed-polyanion cathodes for lithium and sodium rechargeable batteries: combined first principles calculations and experimental study. J Am Chem Soc 134:10369–10372
44. Recham N, Chotard JN et al (2009) Ionothermal synthesis of sodium-based fluorophosphate cathode materials. J Electrochem Soc 156:A993–A999
45. Ellis BL, Makahnouk WRM et al (2010) Crystal structure and electrochemical properties of A_2MPO_4F Fluorophosphates (A = Na, Li; M = Fe, Mn Co, Ni). Chem Mater 22:1059–1070
46. Kawabe Y, Yabuuchi N et al (2011) Synthesis and electrode performance of carbon coated Na_2FePO_4F for rechargeable Na batteries. Electrochem Commun 13:1225–1228
47. Wessells CD, McDowell MT et al (2012) Tunable reaction potentials in open framework nanoparticle battery electrodes for grid-scale energy storage. ACS Nano 6:1688–1694
48. Qian J, Zhou M et al (2012) Nanosized $Na_4Fe(CN)_6$/C composite as a low-cost and high-rate cathode material for sodium-ion batteries. Adv Energy Mater 2:410–414
49. Besenhard JO (1976) The electrochemical preparation and properties of ionic alkali metal- and NR4-graphite intercalation compounds in organic electrolytes. Carbon 14:111–115
50. Ge P, Fouletier M (1988) Electrochemical intercalation of sodium in graphite. Solid State Ionics 28–30(Part 2):1172–1175
51. Doeff MM, Ma YP et al (1993) Electrochemical insertion of sodium into carbon. J Electrochem Soc 140:L169–L170
52. Thomas P, Billaud D (2000) Effect of mechanical grinding of pitch-based carbon fibers and graphite on their electrochemical sodium insertion properties. Electrochim Acta 46:39–47
53. Alcantara R, Jimenez-Mateos JM et al (2001) Carbon black: a promising electrode material for sodium-ion batteries. Electrochem Commun 3:639–642
54. Thomas P, Ghanbaja J et al (1999) Electrochemical insertion of sodium in pitch-based carbon fibres in comparison with graphite in $NaClO_4$-ethylene carbonate electrolyte. Electrochim Acta 45:423–430
55. Thomas P, Billaud D (2001) Sodium electrochemical insertion mechanisms in various carbon fibres. Electrochim Acta 46:3359–3366
56. Stevens DA, Dahn JR (2000) High capacity anode materials for rechargeable sodium-ion batteries. J Electrochem Soc 147:1271–1273
57. Alcantara R, Lavela P et al (2005) Carbon microspheres obtained from resorcinol-formaldehyde as high-capacity electrodes for sodium-ion batteries. Electrochem Solid-State Lett 8:A222–A225
58. Cao Y, Xiao L et al (2012) Sodium ion insertion in hollow carbon nanowires for battery applications. Nano Lett 12:3783–3787
59. Komaba S, Murata W et al (2011) Electrochemical Na insertion and solid electrolyte interphase for hard-carbon electrodes and application to Na-ion batteries. Adv Funct Mater 21:3859–3867
60. Stevens DA, Dahn JR (2000) An in situ small-angle X-ray scattering study of sodium insertion into a nanoporous carbon anode material within an operating electrochemical cell. J Electrochem Soc 147:4428–4431
61. Stevens DA, Dahn JR (2001) The mechanisms of lithium and sodium insertion in carbon materials. J Electrochem Soc 148:A803–A811
62. Xiao L, Cao Y et al (2012) High capacity, reversible alloying reactions in SnSb/C nanocomposites for Na-ion battery applications. Chem Commun 48:3321–3323

63. Chevrier VL, Ceder G (2011) Challenges for Na-ion negative electrodes. J Electrochem Soc 158:A1011–A1014
64. Jow TR, Shacklette LW et al (1987) The role of conductive polymers in alkali-metal secondary electrodes. J Electrochem Soc 134:1730–1733
65. Xu Y, Zhu Y et al (2013) Electrochemical performance of porous carbon/tin composite anodes for sodium-ion and lithium-ion batteries. Adv Energy Mater 3:128–133
66. Komaba S, Matsuura Y et al (2012) Redox reaction of Sn-polyacrylate electrodes in aprotic Na cell. Electrochem Commun 21:65–68
67. Qian J, Chen Y et al (2012) High capacity Na-storage and superior cyclability of nanocomposite Sb/C anode for Na-ion batteries. Chem Commun 48:7070–7072
68. Wu L, Pei F et al (2013) SiC–Sb–C nanocomposites as high-capacity and cycling-stable anode for sodium-ion batteries. Electrochim Acta 87:41–45
69. Chadwick AV, Savin SLP et al (2007) Formation and oxidation of nanosized metal particles by electrochemical reaction of Li and Na with $NiCo_2O_4$: X-ray absorption spectroscopic study. J Phys Chem C 111:4636–4642
70. Alcantara R, Jaraba M et al (2002) $NiCo_2O_4$ spinel: First report on a transition metal oxide for the negative electrode of sodium-ion batteries. Chem Mater 14:2847–2848
71. Kuroda Y, Kobayashi E et al (2010) Electrochemical properties of spinel-type oxide anodes in sodium-ion battery. In: 218th ECS meeting abstract #389
72. Nishijima M, Gocheva ID et al (2009) Cathode properties of metal trifluorides in Li and Na secondary batteries. J Power Sources 190:558–562
73. Kim TB, Choi JW et al (2007) Electrochemical properties of sodium/pyrite battery at room temperature. J Power Sources 174:1275–1278
74. Xiong H, Slater MD et al (2011) Amorphous TiO_2 nanotube anode for rechargeable sodium ion batteries. J Phys Chem C 2:2560–2565
75. Senguttuvan P, Rousse G et al (2011) $Na_2Ti_3O_7$: lowest voltage ever reported oxide insertion electrode for sodium ion batteries. Chem Mater 23:4109–4111
76. Wang W, Yu CJ et al (2013) Single crystalline $Na_2Ti_3O_7$ rods as an anode material for sodium-ion batteries. RSC Adv 3:1041–1044
77. Andersson S, Wadsley AD (1961) The crystal structure of $Na_2Ti_3O_7$. Acta Crystallogr A 14:1245–1249